Evidence for a Crucial Role Played by Oxygen Vacancies in $LaMnO_3$ Resistive Switching Memories

Zhong-tang Xu, Kui-juan Jin, Lin Gu, Yu-ling Jin, Chen Ge, Can Wang, Hai-zhong Guo, Hui-bin Lu, Rui-qiang Zhao, and Guo-zhen Yang*

$LaMnO_3$ (LMO) films are deposited on $SrTiO_3$:Nb (0.8 wt%) substrates under various oxygen pressures to obtain different concentrations of oxygen vacancies in the films. The results of X-ray diffraction verify that with a decrease of the oxygen pressure, the c-axis lattice constant of the LMO films becomes larger, owing to an increase of the oxygen vacancies. Aberration-corrected annular-bright-field scanning transmission electron microscopy with atomic resolution and sensitivity for light elements is used, which clearly shows that the number of oxygen vacancies increases with the decrease of oxygen pressure during fabrication. Correspondingly, the resistive switching property becomes more pronounced with more oxygen vacancies in the LMO films. Furthermore, a numerical model based on the modification of the interface property induced by the migration of oxygen vacancies in these structures is proposed to elucidate the underlying physical origins. The calculated results are in good agreement with the experimental data, which reveal from a theoretical point of view that the migration of oxygen vacancies and the variation of the Schottky barrier at the interface with applied bias dominate the resistive switching characteristic. It is promising that the resistive switching property in perovskite oxides can be manipulated by controlling the oxygen vacancies during fabrication or later annealing in an oxygen atmosphere.

1. Introduction

Conventional semiconductor memory technologies, including dynamic random-access memory (DRAM) and flash memories, are rapidly approaching their bottleneck to continue scaling down beyond a 16 nm threshold,[1] due to the fact that the operation of such devices is established on charge storage which leads to major difficulties in information storage and retrieval for the shrinking cells.[2] Motivated by the exploration of alternatives with improved functionality over conventional memories, extensive investigations of intriguing novel memory concepts have been carried out up to now, which range from phase-change RAM (PCRAM)[3,4] and ferroelectric-related RAM[5–8] (FeRAM) to resistive switching RAM (RRAM).[9–16] Among all these proposed concepts, robust RRAM with great potential for high-density, high-speed, nondestructive readout and nonvolatility is one of the most promising candidates for the next-generation memories and has attracted considerable attention.[17]

In general, the RRAM device has a simple capacitor-like structure with a metal/insulator (or semiconductor)/metal (MIM) stack. The basic operating principle is that the resistance state can be switched between high and low states with the application of an external electric stimulus. A large variety of materials have shown resistive switching properties.[17] In particular, transition metal oxides,[18,19] in

Dr. Z. Xu, Prof. K. Jin, Prof. L. Gu, Dr. Y. Jin, Dr. C. Ge, Dr. C. Wang, Dr. H. Guo, Prof. H. Lu, Dr. R. Zhao, G. Yang
Beijing National Laboratory for Condensed Matter Physics Institute of Physics
Chinese Academy of Science
Beijing 100190, China
E-mail: kjjin@iphy.ac.cn

DOI: 10.1002/smll.201101796

 © 2012 Wiley-VCH Verlag GmbH & Co. KGaA, Weinheim

which complex combinations of charge-, spin-, and orbital-ordered states appear,[20] occupy an important position in this emerging field,[21] offering opportunities for further integration of potential multifunctionality into one device.

At present, a common perspective for the underlying physical origins of the resistive switching phenomenon in transition metal oxides is that the migration of oxygen vacancies (or oxygen ions) plays a dominant role, thereby giving rise to the modification of the interface barrier[18] or inducing the occurrence of the redox process.[22] So far, the important role played by oxygen vacancies in resistive switching has been widely discussed in many previous works.[23–32] However, it would be more attractive and convincing to directly map out the oxygen vacancies by an electron microscope technique with a high resolution, and more direct proof of whether oxygen vacancies are responsible for resistive switching would be crucial for further development of RRAM.[17] Thus, much effort is still needed to advance toward real-product implementation, especially after clearly clarifying the fundamental origins.

Herein, we present a comparative study carried out systematically to reveal the crucial role played by oxygen vacancies in the resistive switching property in $LaMnO_3$ (LMO) films. LMO films, a typical perovskite oxide material, were deposited on $SrTiO_3$:Nb (SNTO, 0.8 wt%) substrates under various oxygen pressures to obtain LMO films with different concentrations of oxygen vacancies. The results from synchrotron-based X-ray diffraction (SXRD) verified that with a decrease of the oxygen pressure the *c*-axis lattice constant of LMO films becomes larger, owing to an increase of the oxygen vacancies. To further characterize the concentration of oxygen vacancies and the structural evolution of these LMO films at atomic sensitivity, sophisticated aberration-corrected scanning transmission electron microscopy (STEM) was utilized, which directly confirmed that with a decrease of the oxygen pressure during fabrication, the number of oxygen vacancies increased. Meanwhile, measurements on the resistive switching showed that a larger variation of resistance can be obtained with a forward and reverse bias in LMO films with more oxygen vacancies. It is thus concluded that oxygen vacancies play a dominant role in RRAM devices composed of transition metal oxides. Furthermore, a numerical model based on modification of the interface property induced by the migration of oxygen vacancies is proposed to elucidate the underlying physical origins of resistive switching. Based on the present results, it is promising that the RRAM property in the perovskite oxides could be manipulated by controlling the oxygen vacancies during fabrication or later annealing in an oxygen atmosphere.

2. Results and Discussion

Figure 1 shows the results of SXRD of LMO films fabricated under various oxygen pressures. The diffraction peaks of the LMO films shift towards smaller diffraction angles with a decrease of the oxygen pressure. The calculated *c*-axis lattice constants of the LMO films fabricated under oxygen

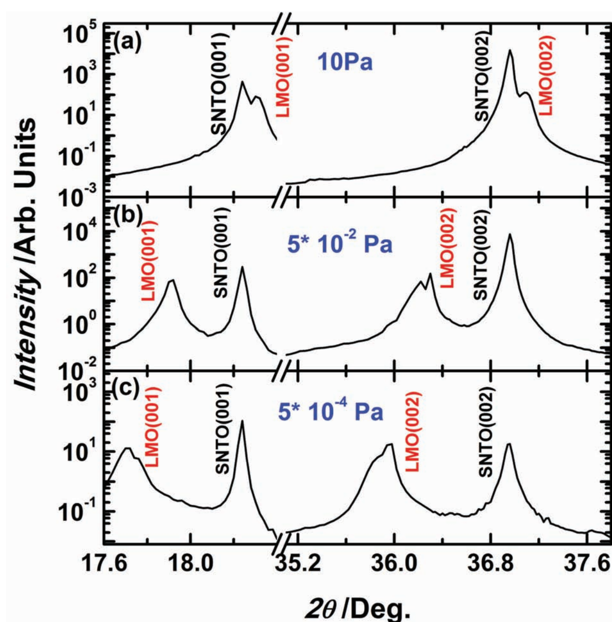

Figure 1. SXRD patterns for LMO thin films fabricated under oxygen pressures of a–c) 10, 5×10^{-2}, and 5×10^{-4} Pa, respectively.

pressures of 10, 5×10^{-2}, and 5×10^{-4} Pa are 3.892, 3.973, and 4.014 Å, respectively. We attribute the modification of the lattice constants to the influence of the oxygen vacancies, naturally produced during the laser molecular beam epitaxy (LMBE) processes.[33] Manganese ions vary from high to low valence states due to the existence of oxygen vacancies, thus leading to a larger manganese ionic radius and a larger lattice constant.[34] It is worth mentioning that similar phenomena of enlarged lattice constants induced by oxygen vacancies have also been observed in previous works.[34–36] In other words, a larger *c*-axis lattice constant corresponds to a larger number of oxygen vacancies, which could be induced by structural distortions in the thin films fabricated under a lower oxygen pressure.

Recent developments of aberration-corrected electron optics have significantly enhanced microscope performance, thus enabling identification of individual light atoms such as oxygen.[37–39] In this study, we exploited an aberration-corrected annular-bright-field (ABF) imaging technique, which is extremely sensitive to the presence of oxygen vacancies. **Figure 2**a–c display typical cross-sectional ABF micrographs obtained from the LMO/SNTO junction viewed along the [001] axis. La as well as Mn and O sites are clearly visible, which can be distinguished according to the image contrast. La is represented as the darkest spots, whereas O is the lightest. These images reveal that the LMO film was epitaxially grown on the *c*-SNTO substrate. Under extreme O depletion conditions, however, the LMO thin film exhibits substantial structural distortions, possibly leading to the formation of lattice defects as shown in Figure 2c. Line profiles along the vertical direction with the markers exhibited in Figure 2a–c are shown in Figure 2d–f, respectively. Note that the O sites are marked with red arrows and the red/blue disks display stacking sequences of O–Mn with

© 2012 Wiley-VCH Verlag GmbH & Co. KGaA, Weinheim

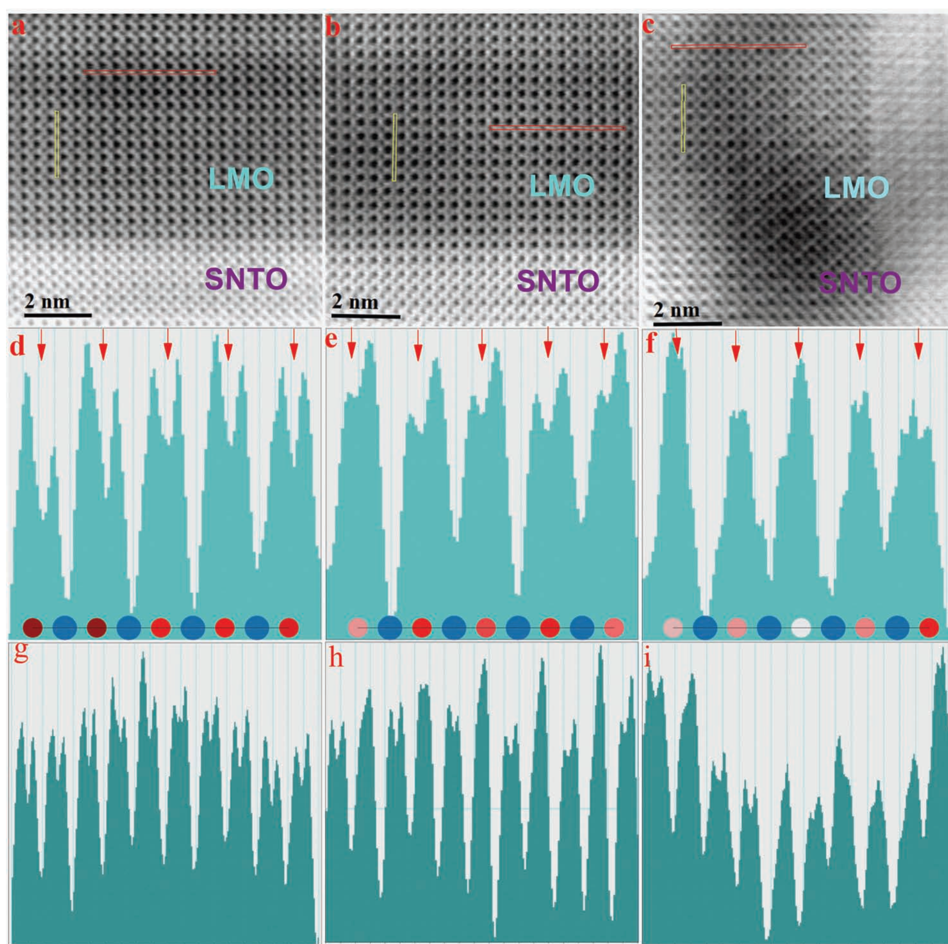

Figure 2. a–c) ABF micrographs of the LMO/SNTO interfaces along the [001] axis corresponding to oxygen pressures of 10, 5×10^{-2}, and 5×10^{-4} Pa, respectively. Note that La is represented by the darkest spots, whereas O is the lightest. d–f) Line profiles along the vertical direction with respect to the markers shown in (a–c). The O sites are marked with red arrows. The red/blue disks display stacking sequences of O–Mn; lighter red ones stand for the presence of O vacancies. g–i) Line profiles along the horizontal direction with respect to the markers shown in (a–c).

lighter red ones standing for the presence of O vacancies. Line profiles along the horizontal direction are shown in Figure 2g–i, together with the profiles in Figure 2d–f. The oxygen vacancy concentration is possibly controlled by the growth kinetics.[40,41] Herein, it is confirmed that the number of oxygen vacancies increases with a decrease of the oxygen pressure for our samples, consistent with the SXRD measurements.

Figure 3 displays typical measured current–voltage (I–V) characteristics of LMO films under various oxygen pressures with Pt as top electrode (TE), and the inset exhibits the schematic setup for I–V measurements. The forward bias is defined by the current flowing from the TE to the SNTO bottom electrode (BE). The voltage bias was scanned as $1 \rightarrow 2 \rightarrow 3 \rightarrow 4$, as shown in Figure 3. Obviously, the switching hysteresis under forward bias is more pronounced than that under reverse bias. A forward bias sweeping tunes the memory into a high-resistance state (HRS or OFF), while a reverse bias sweeping switches the memory into a low-resistance state (LRS or ON). Figure 3 clearly shows that a larger loop of I–V curve can be obtained in LMO films fabricated under a lower oxygen pressure. The resistance changes under the electric field, which demonstrates that larger resistive switching can be obtained in the LMO films with more oxygen vacancies under a sustained bias.

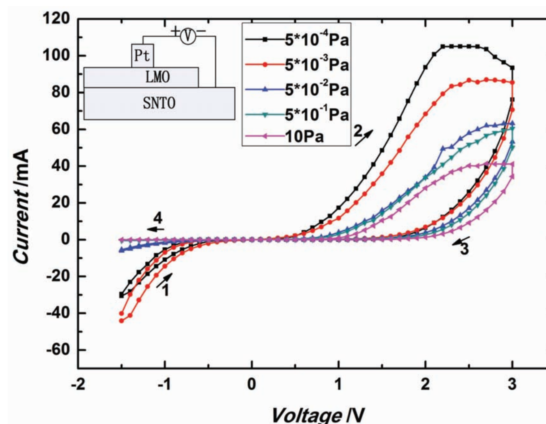

Figure 3. Typical I–V curves for Pt/LMO/SNTO devices under oxygen pressures of 10, 5×10^{-1}, 5×10^{-2}, 5×10^{-3}, and 5×10^{-4} Pa. The direction of bias sweeping is indicated by arrows. The inset shows the measurement configuration of the devices.

© 2012 Wiley-VCH Verlag GmbH & Co. KGaA, Weinheim

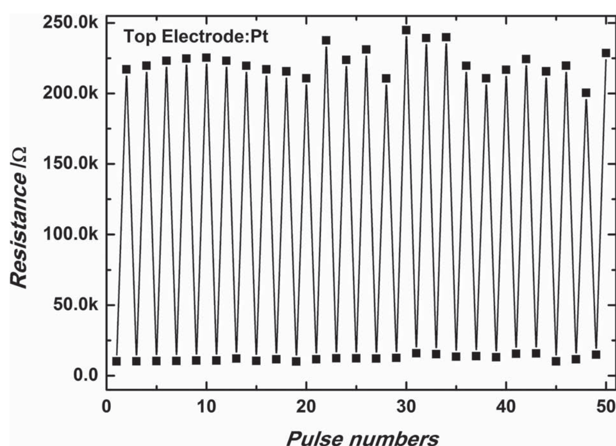

Figure 4. Pulse measurements of the Pt/LMO/SNTO devices with a fabrication oxygen pressure of 5×10^{-4} Pa. The pulse condition for the HRS is +5 V with a pulse width of 1 ms and for the LRS is −5 V with a pulse width of 1 ms. The resistance was read out at 0.1 μA.

To evaluate the stability of the devices, we performed pulse endurance measurements. The results for the Pt/LMO/SNTO structure fabricated under an oxygen pressure of 5×10^{-4} Pa are shown in **Figure 4**. Bistable HRS/LRS switching was achieved by applying a pulse voltage of +5 and –5 V with a 1 ms width for reset (LRS to HRS) and set (HRS to LRS) operations. The resistance was then read out with a read current of 0.1 μA. It was observed that stable HRS and LRS states were achieved with an R_{OFF}/R_{ON} ratio of about 18, and no significant change of the resistance ratio was observed during pulse measurements. With further increase of the number of cycles, the devices show no significant resistance decay in both the HRS and LRS.

From **Figure 5** we can see that the R_{OFF}/R_{ON} ratio indicated by numbers becomes larger with the decrease of the oxygen pressure, except for the LMO film with the largest number of oxygen vacancies, that is, the film fabricated under 5×10^{-4} Pa oxygen pressure. We think this is due to the excessive structural distortion associated with too many oxygen vacancies for the LMO films fabricated under 5×10^{-4} Pa oxygen pressure, which can be verified by the ABF micrograph shown in Figure 2c. According to the detailed characterization of SXRD and aberration-corrected STEM, it is known that for the structures fabricated under a lower oxygen pressure there are more oxygen vacancies. Therefore, more free carriers and mobile oxygen vacancies are obtained for the films fabricated under a lower oxygen pressure, which induce a larger current and R_{OFF}/R_{ON} ratio. In other words, the resistive switching property becomes more pronounced in the films containing more oxygen vacancies. This is direct experimental evidence for the crucial role played by oxygen vacancies in resistive switching.

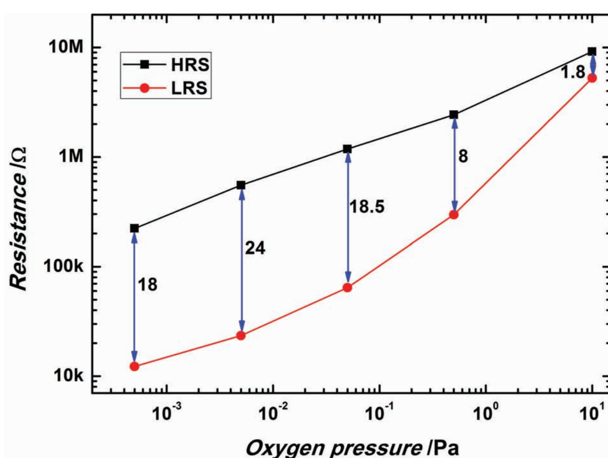

Figure 5. Dependence of the HRS and LRS on the fabrication oxygen pressure. The R_{OFF}/R_{ON} ratios are indicated by numbers.

To theoretically reveal the underlying physical origins, we propose a numerical approach based on the oxygen vacancy migration model. Detailed descriptions of the numerical model can be found in the Supporting Information. The oxygen-deficient LMO is usually regarded as an n-type semiconductor, because the oxygen vacancies act as donors in oxides and become positively charged after releasing electrons to the conduction band.[42] The work functions of Pt and SNTO are about 5.3[43] and 4.05 eV,[44] respectively. Therefore, ohmic contact can be formed at the interface of LMO/SNTO, and the Schottky barrier at the interface between Pt and LMO will dominate the transport property of the entire system. Hence, it is proposed that there exists an evolution of several states for Pt/LMO/SNTO according to the number of oxygen vacancies at the Pt/LMO Schottky interface under the electric field. When a negative voltage is applied on the TE, the oxygen vacancies will accumulate at the Pt/LMO interface, which makes the doping density at the interface increase, while the oxygen vacancies will migrate away from the Pt/LMO interface, thereby giving rise to a decrease of doping density under the forward bias. The variation of the carrier concentration due to the oxygen vacancy migration will result in different states at the Pt/LMO Schottky barrier, which causes high and low resistance states.

Because of the unobvious resistive switching property under the reverse bias, only one state is taken into account in the reverse bias for simplicity. Thus, we regard the system as an evolution of three states, S1, S2, and S3, in the whole bias sweeping process as shown in **Figure 6**. The necessary parameters for calculations are listed in **Table 1**. The doping density of as-grown LMO (5×10^{-3} Pa) film is measured as 3.5×10^{19} cm^{-3} with a Quantum Design physical property measurement system (PPMS-9). The bandgap of the LMO film is 1.6–2.0 eV as reported by previous works.[45–48] With the decrease of the doping density, the bandgap becomes larger according to the well-known bandgap narrowing effect,[49] and the carrier mobility will become larger. The theoretical results are in good agreement with the experimental data, as shown in Figure 6, which reveals from a theoretical point of view that the migration of oxygen vacancies and the variation of the Schottky barrier at the interface with applied bias dominate the resistive switching property.

The band structures of S2 and S3, which are the states of Pt/LMO/SNTO before and after applying forward bias, respectively, are shown in **Figure 7**. It can be seen that for state S3 the width of the depletion region becomes wider and the barrier height becomes larger compared with S2. In this

© 2012 Wiley-VCH Verlag GmbH & Co. KGaA, Weinheim

small NANO MICRO

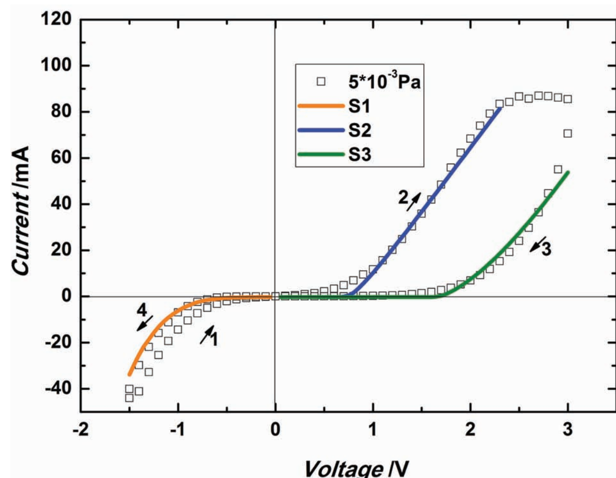

Figure 6. Calculated *I–V* curves of states S1, S2, and S3 (solid lines) compared with measured *I–V* curves (open squares) of the structure fabricated under an oxygen pressure of 5×10^{-3} Pa. Arrows indicate the direction of bias sweeping.

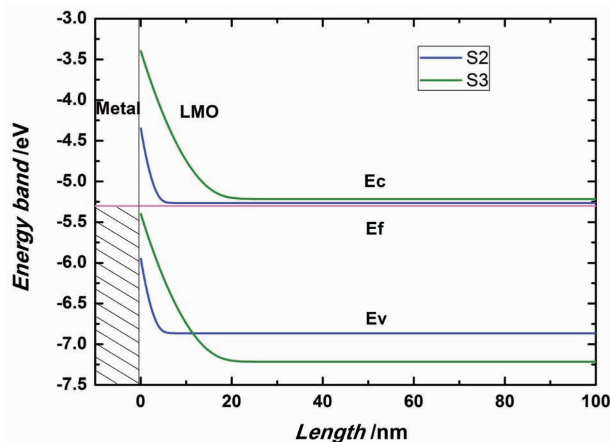

Figure 7. Calculated band structures of S2 and S3. E_c, E_v, and E_f represent the conduction band, the valence band, and the Fermi level of LMO, respectively.

simplified model, we only consider the homogeneous oxygen vacancy distribution at the Pt/LMO interface. The dynamic inhomogeneous distributions of oxygen vacancies should be further investigated for the resistive switching phenomenon in the future.

3. Conclusion

We have designed a series of comparative experiments for LMO films fabricated under various oxygen pressures, and proved a dominant role of oxygen vacancies in the resistive switching property. The results of SXRD verified that with a decrease of the oxygen pressure the *c*-axis lattice constant of LMO films becomes larger, owing to an increase of the oxygen vacancies. Aberration-corrected STEM was utilized to further characterize the structure of the LMO films with atomic sensitivity, which directly confirmed that with a decrease of the oxygen pressure the number of oxygen vacancies becomes larger. Correspondingly, larger resistive switching can be obtained in LMO films with more oxygen vacancies under a sustained bias, while a consistent condition is obtained under pulse bias except for the LMO film with the largest number of oxygen vacancies, the film fabricated under 5×10^{-4} Pa oxygen pressure, due to excessive structure distortion associated with too many oxygen vacancies. The resistive switching property becomes more pronounced with LMO films containing more oxygen vacancies. Furthermore, a numerical model based on the modification of the interface barrier induced by the migration of oxygen vacancies is proposed to elucidate the physical origins. The calculated results are in good agreement with the experimental data, which reveal from a theoretical point of view that the migration of oxygen vacancies and the variation of Schottky barrier at the interface with applied bias dominate the resistive switching characteristic. It is promising that the RRAM property in perovskite oxides could be manipulated by controlling the oxygen vacancies during fabrication or later annealing in an oxygen atmosphere.

Table 1. Overview of the parameters used in the calculations.

	S1	S2	S3
concentration [cm^{-3}]	9.8×10^{19}	3.5×10^{19}	5×10^{18}
mobility [cm^2 (V s)$^{-1}$]	1.5	2	7
bandgap [eV]	1.55	1.6	2.0

4. Experimental Section

Sample Preparation: LMO thin films were epitaxially grown on SNTO (001) substrates with 3 × 5 mm size and 0.5 mm thickness by computer-controlled LMBE with a pulsed XeCl excimer laser beam (≈20 ns, 2 Hz, ≈1.5 J cm^{-2}) focused on a sintered ceramic LMO target. The SNTO substrates were carefully cleaned with alcohol, acetone, and deionized water before fabrication. Subsequently, LMO films with a thickness of 100 nm were deposited at 750 °C under oxygen pressures of 5×10^{-4}, 5×10^{-3}, 5×10^{-2}, 5×10^{-1} and 10 Pa, and then annealed in situ under the same conditions for 20 min before cooling to room temperature in an oxygen atmosphere.

Characterization: The crystal structure was identified by high-resolution synchrotron X-ray diffractometry by the BL14B1 beam line of Shanghai Synchrotron Radiation Facility (SSRF), using 1.24 Å X-rays with a Huber 5021 six-axes diffractometer.

Aberration-corrected STEM was performed using a 2100F transmission electron microscope operated at an acceleration voltage of 200 keV (JEOL, Tokyo, Japan). A CEOS probe-forming aberration corrector provided the ABF images with a spatial resolution better than 0.1 nm.

Electrical Characteristics: The dc and pulsed current–voltage (*I–V*) characteristics were measured by a Keithley 2400 source meter and Tektronix AFG320 arbitrary function generator at room temperature. The inset of Figure 3 shows the schematic setup for

 © 2012 Wiley-VCH Verlag GmbH & Co. KGaA, Weinheim

I–V measurements. During the measurements, a bias was applied to the TE (Pt), whereas the BE (SNTO) was grounded. To protect devices, the applied voltage was restricted from −1.5 to +3 V.

Supporting Information

Supporting Information is available from the Wiley Online Library or from the author.

Acknowledgements

This work was supported by the National Basic Research Program of China (No. 2012CB921403) and the National Natural Science Foundation of China (No. 10825418 and No. 11134012). The XRD measurement was supported by the Shanghai Synchrotron Radiation Facility (SSRF).

[1] International Technology Roadmap for Semiconductors, available at www.itrs.net.
[2] P. Zubko, J. M. Triscone, *Nature* **2009**, *460*, 45.
[3] M. H. R. Lankhorst, B.W. S. M. M. Ketelaars, R. A. M. Wolters, *Nat. Mater.* **2005**, *4*, 347.
[4] S. Lai, T. Lowrey, *IEEE IEDM 2001 Tech. Dig.* **2011**, *36*, 5.
[5] R. Meyer, R. Waser, *J. Appl. Phys.* **2006**, *100*, 051611.
[6] a) A. Q. Jiang, C. Wang, K. J. Jin, X. B. Liu, J. F. Scott, C. S. Hwang, T. A. Tang, H. B. Lu, G. Z. Yang, *Adv. Mater.* **2011**, *23*, 1277; b) C. Wang, K. J. Jin, Z. T. Xu, L. Wang, C. Ge, H. B. Lu, H. Z. Guo, M. He, G. Z. Yang, *Appl. Phys. Lett.* **2011**, *98*, 192901.
[7] R. C. G. Naber, K. Asadi, P. W. M. Blom, D. M. de Leeuw, B. de Boer, *Adv. Mater.* **2010**, *22*, 933.
[8] V. Garcia, S. Fusil, K. Bouzehouane, S. Enouz-Vedrenne, N. D. Mathur, A. Barthelemy, M. Bibes, *Nature* **2009**, *460*, 81.
[9] A. Asamitsu, Y. Tomioka, H. Kuwahara, Y. Tokura, *Nature* **1997**, *388*, 50.
[10] S. Q. Liu, N. J. Wu, A. Ignatiev, *Appl. Phys. Lett.* **2000**, *76*, 2749.
[11] K. Szot, W. Speier, G. Bihlmayer, R. Waser, *Nat. Mater.* **2006**, *5*, 312.
[12] R. Waser, M. Aono, *Nat. Mater.* **2007**, *6*, 833.
[13] D. B. Strukov, G. S. Snider, D. R. Stewart, R. S. Williams, *Nature* **2008**, *453*, 80.
[14] Z. T. Xu, K. J. Jin, C. Wang, H. B. Lu, C. Wang, L. Wang, G. Z. Yang, *Appl. Phys. A* **2011**, *105*, 149.
[15] R. Muenstermann, T. Menke, R. Dittmann, R. Waser, *Adv. Mater.* **2010**, *22*, 4819.
[16] D. Strukov, J. Borghetti, R. Williams, *Small* **2009**, *5*, 1058.
[17] G. I. Meijer, *Science* **2008**, *319*, 1625.
[18] A. Sawa, *Mater. Today* **2008**, *11*, 28.
[19] S. F. Karg, G. I. Meijer, J. G. Bednorz, C. T. Rettner, A. G. Schrott, E. A. Joseph, C. H. Lam, M. Janousch, U. Staub, F. La Mattina, S. F. Alvarado, D. Widmer, R. Stutz, U. Drechsler, D. Caimi, *IBM J. Res. Dev.* **2008**, *52*, 481.
[20] Y. Tokura, N. Nagaosa, *Science* **2000**, *288*, 462.
[21] H. Takagi, H. Y. Hwang, *Science* **2010**, *327*, 1601.
[22] R. Waser, R. Dittmann, G. Staikov, K. Szot, *Adv. Mater.* **2009**, *21*, 2632.
[23] M. Janousch, G. I. Meijer, U. Staub, B. Delley, S. F. Karg, B. P. Andreasson, *Adv. Mater.* **2007**, *19*, 2232.
[24] Y. B. Nian, J. Strozier, N. J. Wu, X. Chen, A. Ignatiev, *Phys. Rev. Lett.* **2004**, *92*, 178302.
[25] K. Shibuya, R. Dittmann, S. B. Mi, R. Waser, *Adv. Mater.* **2010**, *22*, 411.
[26] Y. B. Nian, J. Strozier, N. J. Wu, X. Chen, A. Ignatiev, *Phys. Rev. Lett.* **2007**, *98*, 146403.
[27] C. Y. Lin, C. Y. Wu, C. Y. Wu, T. C. Lee, F. L. Yang, C. Hu, T. Y. Tseng, *IEEE Electron Device Lett.* **2007**, *28*, 366.
[28] J. J. Yang, M. D. Pickett, X. M. Li, D. A. A. Ohlberg, D. R. Stewart, R. S. Williams, *Nat. Nanotechnol.* **2008**, *3*, 429.
[29] S. Asanuma, H. Akohj, *Phys. Rev. B* **2009**, *80*, 235113.
[30] M. K. Yang, J. W. Park, T. K. Ko, J. K. Lee, *Appl. Phys. Lett.* **2009**, *95*, 042105.
[31] D. S. Jeong, H. Schroeder, U. Breuer, R. Waser, *J. Appl. Phys.* **2008**, *104*, 123716.
[32] J. W. Parka, J. W. Park, K. Jung, M. K. Yang, J. K. Leeb, *J. Vac. Sci. Technol. B* **2006**, *24*, 2205.
[33] W. Siemons, G. Koster, H. Yamamoto, W. A. Harrison, G. Lucovsky, T. H. Geballe, D. H. A. Blank, M. R. Beasley, *Phys. Rev. Lett.* **2007**, *98*, 196802.
[34] L. Qiao, X. F. Bi, *Thin Solid Films* **2010**, *529*, 943.
[35] H. L. Cai, X. S. Wu, J. Gao, *Chem. Phys. Lett.* **2009**, *467*, 313.
[36] S. B. Mi, C. L. Jia, T. Heeg, O. Trithaveesak, J. Schubert, K. Urban, *J. Cryst. Growth* **2005**, *283*, 425.
[37] C. L. Jia, K. Urban, *Science* **2004**, *303*, 2001.
[38] S. D. Findlay, N. Shibata, H. Sawada, E. Okunishi, Y. Kondo, Y. Ikuhara, *Ultramicroscopy* **2010**, *110*, 903.
[39] O. L. Krivanek, M. F. Chisholm, V. Nicolosi, T. J. Pennycook, G. J. Corbin, N. Dellby, M. F. Murfitt, Ch. S. Own, Z. S. Szilagyi, M. P. Oxley, S. T. Pantelides, S. J. Pennycook, *Nature* **2010**, *464*, 571.
[40] S. Miyoshia, J. O. Honga, K. Yashir, A. Kaimaia, Y. Nigaraa, K. Kawamurab, T. Kawadaa, J. Mizusakia, *Solid State Ionics* **2003**, *161*, 209.
[41] J. H. Kuo, H. U. Anderson, D. M. Sparlin, *J. Solid State Chem.* **1989**, *83*, 52.
[42] S. R. Basu, L. W. Martin, Y. H. Chu, M. Gajek, R. Ramesh, R. C. Rai, X. Xu, J. L. Musfeldt, *Appl. Phys. Lett.* **2008**, *92*, 091905.
[43] M. Minohara, I. Ohkubo, H. Kumigashira, M. Oshima, *Appl. Phys. Lett.* **2007**, *90*, 132123.
[44] a) P. Han, K. J. Jin, H. B. Lu, Q. L. Zhou, Y. L. Zhou, G. Z. Yang, *Appl. Phys. Lett.* **2007**, *91*, 182102; b) K. J. Jin, H. B. Lu, Q. L. Zhou, K. Zhao, B. L. Cheng, Z. H. Chen, Y. L. Zhou, G. Z. Yang, *Phys. Rev. B* **2005**, *71*, 184428; c) C. L. Hu, K. J. Jin, P. Han, H. B. Lu, L. Liao, G. Z. Yang, *Appl. Phys. Lett.* **2008**, *93*, 162106.
[45] T. Saitoh, A. E. Bocquet, T. Mizokawa, H. Namatame, M. Abbate, Y. Takeda, M. Takano, *Phys. Rev. B* **1995**, *51*, 13942.
[46] D. Fuks, S. Dorfman, J. Felsteiner, L. Bakaleinikov, A. Gordon, E. A. Kotomin, *Solid State Ionics* **2004**, *173*, 107.
[47] M. Hannani, D. Rached, M. Rabah, R. Khenata, N. Benayad, M. Hichour, A. Bouhemadou, *Mater. Sci. Semicond. Process.* **2008**, *11*, 81.
[48] Y. Nohara, S. Yamamoto, T. Fujiwara, *Phys. Rev. B* **2009**, *79*, 195110.
[49] S. M. Sze, *Physica of Semiconductor Devices, Physics and Technology*, 2nd ed., Wiley, New York **2001**.

Received: September 1, 2011
Published online: February 20, 2012

© 2012 Wiley-VCH Verlag GmbH & Co. KGaA, Weinheim